MDPI

Vacuum Electrodeposition of Cu(In, Ga)Se$_2$ Thin Films and Controlling the Ga Incorporation Route

Kanwen Hou [1,3,4], Guohao Liu [1,3,4], Jia Yang [1,2,3,4,*], Wei Wang [1,3,4], Lixin Xia [1,3,4], Jun Zhang [1,3,4], Baoqiang Xu [1,2,3,4] and Bin Yang [1,2,3,4]

1   Key Laboratory for Nonferrous Vacuum Metallurgy of Yunnan Province, Kunming University of Science and Technology, Kunming 650093, China
2   State Key Laboratory of Complex Non-Ferrous Metal Resources Clean Utilization, Kunming University of Science and Technology, Kunming 650093, China
3   National Engineering Research Center of Vacuum Metallurgy, Kunming University of Science and Technology, Kunming 650093, China
4   Faculty of Metallurgical and Energy Engineering, Kunming University of Science and Technology, Kunming 650093, China
*   Correspondence: yangjia0603@163.com

Abstract: The traditional electrochemical deposition process used to prepare Cu(In, Ga)Se$_2$ (CIGS) thin films has inherent flaws, such as the tendency to produce low-conductivity Ga$_2$O$_3$ phase and internal defects. In this article, CIGS thin films were prepared under vacuum (3 kPa), and the mechanism of vacuum electrodeposition CIGS was illustrated. The route of Ga incorporation into the thin films could be controlled in a vacuum environment via inhibiting pH changes at the cathode region. Through the incorporation of a low-conductivity secondary phase, Ga$_2$O$_3$ was inhibited at 3 kPa, as shown by Raman and X-ray photoelectron spectroscopy. The preparation process used a higher current density and a lower diffusion impedance and charge transfer impedance. The films that were produced had larger particle sizes.

1. Introduction

CIGS thin films are one of the most promising photovoltaic materials for second-generation solar cells [1]. They are composite semiconductor materials with chalcopyrite structures [2] with band gaps of 1.0 eV to 1.7 eV [3]. Co-evaporation [4], magnetron sputtering [5], spray pyrolysis [6], solution gel method [7], and electrodeposition [8] are the main methods to prepare CIGS thin films.

Electrodeposition has the advantages of a low preparation cost, high efficiency, large area, and continuous preparation and is likely to be used in future industrialized production methods [9]. However, it has some inherent flaws when used to prepare metal materials. For example, hydrogen is easily generated on the cathode surface and is difficult to remove and the deposition rate can be slow [10,11].

Generally, a vacuum environment induces rapid off-gassing [12] and lower oxidation and contamination [13]. Based on these properties, researchers have conducted studies on the electrodeposition of metal thin films in a vacuum environment. In the 1940s, RCA Company [14] electrodeposited Fe and Mn in a vacuum environment and found that hydrogen quickly escaped from the films, and the oxidation of the film was avoided. This resulted in the preparation of smooth and bright metal films. In 1984, E Muttilainen et al. [15] electrodeposited Cr in a vacuum environment and found that a low-pressure environment increased the current efficiency and reduced the porosity and roughness of the coating. They concluded that low pressure was one of the most important factors affecting the quality of the coating. In a following study, S. E. Nam [16,17],

R. Su [18], and P. Ming et al. [19,20] prepared metal thin films with excellent properties using vacuum electrodeposition.

In the application of electrodeposition to prepare CIGS thin films, the Ga_2O_3 phase is also easily generated, along with the generation of hydrogen on the cathode surface [21,22]. The entry of Ga_2O_3 into the films can decrease the conductivity [23,24]. Therefore, in this article, electrodeposition was applied to prepare CIGS thin films in a vacuum environment. The effects of the vacuum environment on the deposition process and the composition, morphology, and phases in the CIGS thin films were studied.

2. Materials and Methods

The electrolyte solution contained 200 mL deionized water with 4 mM $CuCl_2$, 10 mM $InCl_3$, 10 mM $GaCl_3$, 8 mM H_2SeO_3, and a supporting electrolyte (100 mM LiCl, 100 mM NH_4Cl, and 60 mM NH_2SO_3H). The pH of the solution was adjusted to 1.8 by adding concentrated hydrochloric acid dropwise.

Electrochemical experiments, including linear scanning voltammetry (LSV), potentiostatic polarization, electrochemical impedance spectroscopy (EIS), and electrodeposition were carried out on CIGS thin films in a three-electrode system with a SnO_2/glass (1 × 1.5 cm) as the working electrode, a Pt electrode as the counter electrode, and a saturated calomel electrode (SCE) as the reference electrode.

A CorrTest CH310H electrochemical workstation was used for the LSV, potentiostatic polarization, EIS, and electrodeposition CIGS thin film studies. The LSV curves were measured at potentials between 0.1 V to −1.0 V (vs. SCE) with a scanning rate of 10 mV/s. The potentiostatic polarization curves were measured at a potential of −0.60 V (vs. SCE) and a polarization time of 30 min. EIS was performed at a potential of −0.60 V (vs. SCE) with a test frequency range of 0.01 Hz to 100 kHz. On electrodeposited CIGS thin films, the potential range was −0.1 V to −0.9 V (vs. SCE), and the polarization time was 30 min. When the experiment was carried out at 3 kPa, a vacuum pump was used to extract the air from the experimental system for 30 min. Figure 1 illustrates the electrodeposition process of CIGS thin films.
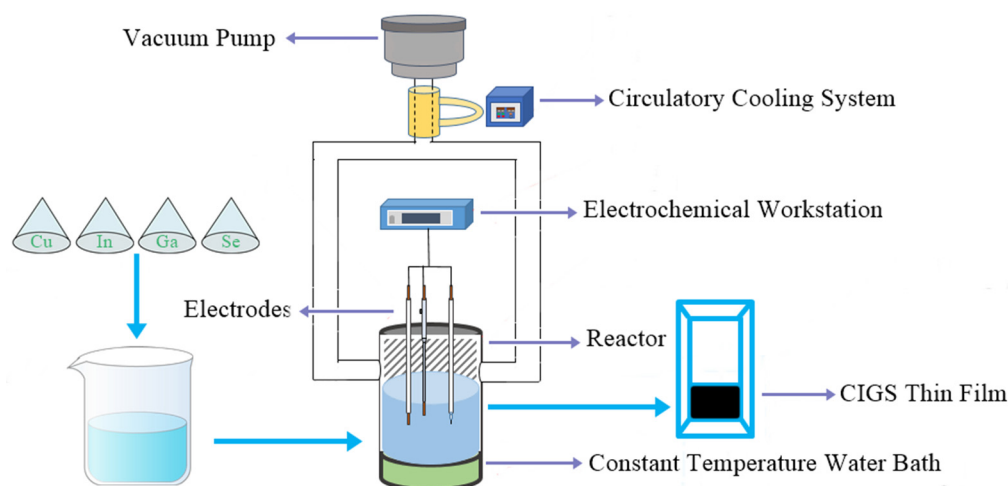
Figure 1. A schematic of the electrodeposition CIGS thin films system.

Scanning electron microscopy (SEM, TM3030Plus, Hitachi, Tokyo, Japan) was used to measure the morphology of CIGS thin films, and energy-dispersive spectroscopy (EDS, TM3030Plus, Hitachi, Tokyo, Japan) was utilized to characterize the elemental composition of the CIGS thin films. X-ray diffraction (XRD, Rigaku Ultima IV, Tokyo, Japan), Raman spectroscopy (Raman, DXRxi, Thermo Scientific, MA, USA), and X-ray photoelectron spectroscopy (XPS, Escalab Xi+, Thermo Scientific, MA, USA) were used to characterize the phases in the CIGS thin films.

3. Results and Discussion

Figure 2 illustrates a schematic of how the vacuum environment affects the electrochemical behavior of Ga^{3+}. In the cathode region, the vacuum environment inhibited the Volmer reaction of H^+ to a hydrogen atom (H_{ads}), leading to lower H^+ consumption on the cathode surface. In the anode region, the oxygen evolution reaction (OER) of H_2O to O_2 was promoted, which produced additional O_2. At the same time, the rapid release of O_2 bubbles agitated the electrolyte solution, which led to a uniform H^+ distribution in the electrolyte solution. Thus, the inhibition of the Volmer reaction and the promotion of the OER together stabilized the pH of the cathode region. This finally interrupted the route of Ga^{3+} entering the films in the form of Ga_2O_3 by the hydrolytic reaction of Ga^{3+}.
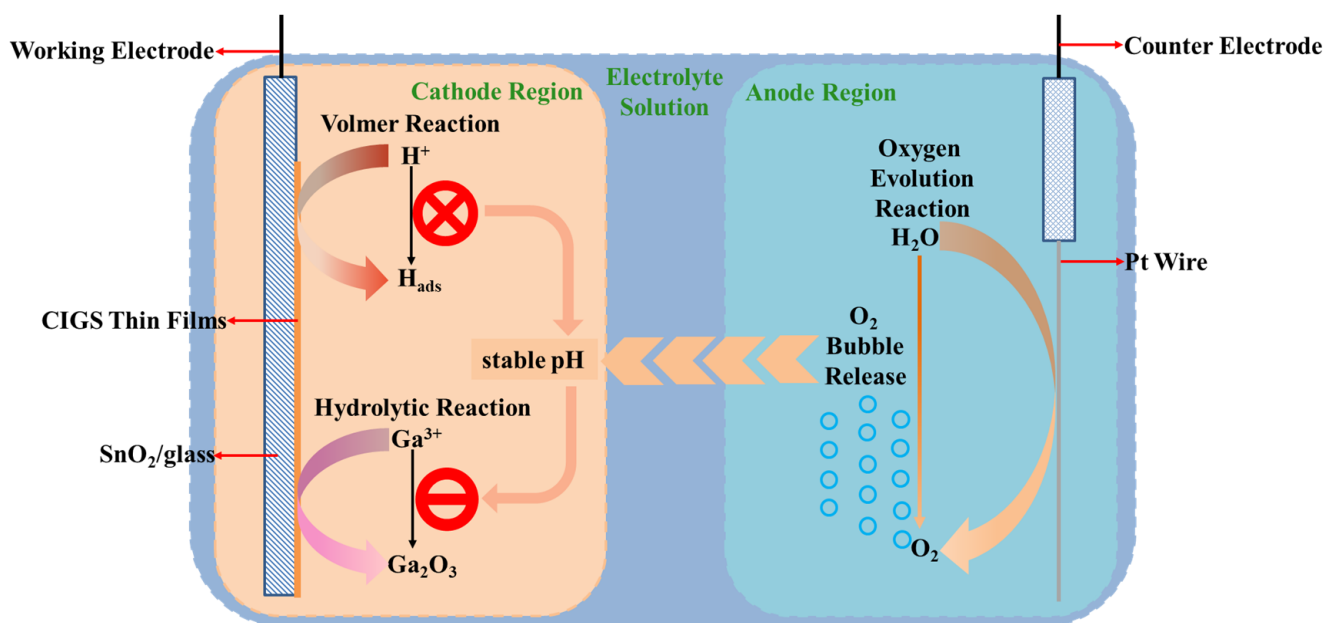

Figure 2. Schematic illustration for the inhibition of Ga^{3+} hydrolysis in 3 kPa.

3.1. LSV Analyses

Figure 3a illustrates the effects of the vacuum environment on the hydrogen evolution potentials. Evidence of an inhibited reaction of H^+ to H_{ads} was found in a vacuum environment. Peak C_1 corresponding to the reaction of H^+ to H_{ads} (Equation (1)) did not appear at 3 kPa, possibly due to a decrease in the H_2 partial pressure. Because of the reduced partial pressure of H_2, the overpotential of H^+/H_{ads} on the electrode surface was increased. This phenomenon has also been observed on Au and Pt electrodes [25,26].

$$H^+ + e^- \rightarrow H_{ads} \tag{1}$$

Figure 3b illustrates the LSV curve of the Cu unary solution at 3 kPa. Peaks C_1, C_2, and C_3 corresponded to the reaction of Cu^{2+} to Cu^+ (Equation (2)), Cu^+ to Cu (Equation (3)), and H^+ to H_{ads} (Equation (1)), respectively [27]. Peak C_1 was indistinguishable at 80 kPa and 3 kPa, indicating that pressure did not affect the reaction of Cu^{2+} to Cu^+. Peak C_2 was reduced at 3 kPa, indicating that the formation of Cu was promoted in a low-pressure environment. Peak C_3 did not appear at 3 kPa, indicating that the reaction of H^+ to H_{ads} was inhibited in a vacuum environment.

$$Cu^{2+} + e^- \rightarrow Cu^+ \tag{2}$$

$$Cu^+ + e^- \rightarrow Cu \tag{3}$$
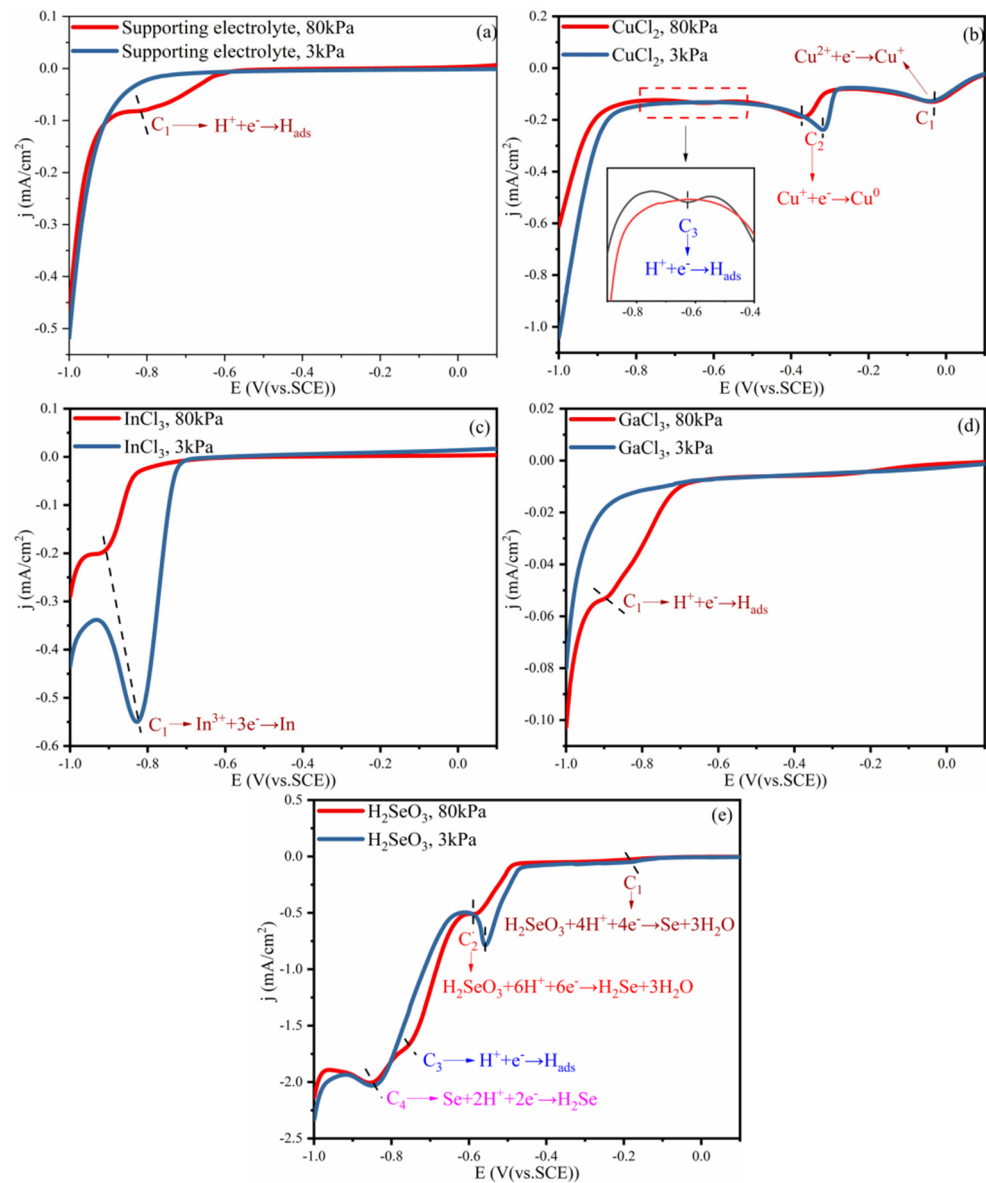
Figure 3. The LSV curves in the (**a**) supporting electrolyte, (**b**) 4 mM $CuCl_2$, (**c**) 10 mM InClsubscript3, (**d**) 10 mM $GaCl_3$, and (**e**) 8 mM H_2SeO_3 unary solutions at 3 kPa.

Figure 3c illustrates the LSV curve of the In unary solution at 3 kPa. Peak C_1 corresponded to the reaction of In^{3+} to In (Equation (4)) [28]. This peak was reduced at 3 kPa, showing that the formation of In was promoted in a vacuum environment.

$$In^{3+} + 3e^- \rightarrow In \tag{4}$$

Figure 3d illustrates the LSV curve of the Ga unary solution at 3 kPa. Peak C_1 corresponds to the reaction of H^+ to H_{ads} [27] (Equation (1)). This peak did not appear at 3 kPa, indicating that the reaction of H^+ to H_{ads} was inhibited in a vacuum environment. The reaction of Ga^{3+} to Ga did not occur within the range of 0.1 V to -1.0 V because the reaction required a higher potential [24].

Figure 3e illustrates the LSV curve of the Se unary solution at 3 kPa. Peaks C_1, C_2, C_3, and C_4 corresponded to the reactions of H_2SeO_3 to Se (Equation (5)), H_2SeO_3 to H_2Se (Equation (6)), H^+ to H_{ads} (Equation (1)), and Se to H_2Se (Equation (7)), respectively [27]. The current densities of peaks C_1, C_2, and C_4 were greater at 3 kPa, indicating that the

formation of H_2Se and Se was promoted. Peak C_3 did not appear at 3 kPa, indicating that the reaction of H^+ to H_{ads} was inhibited in a vacuum environment.

$$H_2SeO_3 + 4H^+ + 4e^- \rightarrow Se + 3H_2O \tag{5}$$

$$H_2SeO_3 + 6H^+ + 6e^- \rightarrow H_2Se + 3H_2O \tag{6}$$

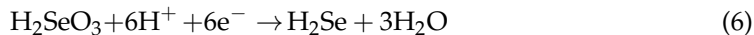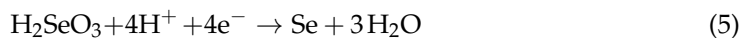$$Se + 2H^+ + 2e^- \rightarrow H_2Se \tag{7}$$

Figure 4a illustrates the LSV curves of Cu-Se binary solutions at 3 kPa. Peaks C_1 and C_2 corresponded to the formation of Cu^+ and Se, respectively (Equations (2) and (5)). Peaks C_3 and C_4 corresponded to the reaction of H_2SeO_3 to H_2Se and Se to H_2Se, respectively (Equations (6) and (7)). Since the solution contained both Cu^+ and Cu^{2+}, the two ions were induced by H_2SeO_3 or H_2Se to form Cu_2Se or $CuSe$, respectively [26] (denoted as Cu_3Se_2 phase) (Equations (8)–(11)). The current densities of peaks C_3 and C_4 were greater at 3 kPa, indicating that the formation of Cu_3Se_2 was promoted in a vacuum environment.
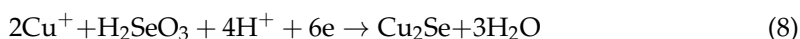
$$2Cu^+ + H_2SeO_3 + 4H^+ + 6e \rightarrow Cu_2Se + 3H_2O \tag{8}$$

$$Cu^{2+} + H_2SeO_3 + 4H^+ + 6e \rightarrow CuSe + 3H_2O \tag{9}$$

$$2Cu^+ + H_2Se \rightarrow Cu_2Se + 2H^+ \tag{10}$$

$$Cu^{2+} + H_2Se \rightarrow CuSe + 2H^+ \tag{11}$$

Figure 4b illustrates the LSV curves of the In-Se binary solutions at 3 kPa. Peaks C_1 and C_2 corresponded to the reaction of H_2SeO_3 to H_2Se and Se to H_2Se, respectively (Equations (6) and (7)). H_2SeO_3 reacted with H_2Se to form Se (Equation (12)). Because In_2Se_3 has a high standard Gibbs energy of formation (-386 kJ/mol [29]), H_2Se induced In^{3+} to form In_2Se_3 [30] (Equation (13)). The current densities of peaks C_1 and C_2 were greater at 3 kPa, indicating that the formation of H_2Se, In_2Se_3, or In was promoted in a vacuum environment.
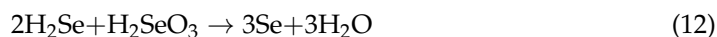
$$2H_2Se + H_2SeO_3 \rightarrow 3Se + 3H_2O \tag{12}$$

$$3H_2Se + 2In^{3+} + 6e^- \rightarrow In_2Se_3 \tag{13}$$

Figure 4c illustrates the LSV curves of Ga-Se binary solutions at 3 kPa. The peaks C_1, C_2, and C_3 correspond to the reaction of H_2SeO_3 to Se, H_2SeO_3 to H_2Se, and Se to H_2Se, respectively (Equations (5)–(7)). Because Ga_2Se_3 has a high standard Gibbs energy of formation (-418 kJ/mol [31]), Ga^{3+} was induced by H_2Se to form Ga_2Se_3 [32] (Equation (14)). The current densities of the peaks C_2 and C_3 are greater at 3 kPa, indicating that the formation of H_2Se or Ga_2Se_3 was promoted in a vacuum environment.
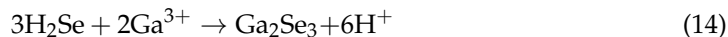
$$3H_2Se + 2Ga^{3+} \rightarrow Ga_2Se_3 + 6H^+ \tag{14}$$

Figure 4d illustrates the LSV curves of Cu-In-Se ternary solutions at 3 kPa. Peaks C_1, C_2, C_3, C_4, and C_6 correspond to the formation of Cu^+, Se, Cu_3Se_2, H_2Se, and In_2Se_3 or In, respectively (Equations (2), (5), (8)–(11), (6), (13) or (4)). In^{3+} was induced by $Cu_3Se_2 + H_2SeO_3$ or $Cu_3Se_2 + H_2Se$ to produce more stable $CuInSe_2$ [32] (Equations (15) and (16)) at peak C_5. As the polarization potential increased, the current density became greater at 3 kPa, indicating that the formation of CIS was promoted in a vacuum environment.

$$3In^{3+} + Cu_3Se_2 + 4H_2SeO_3 + 16H^+ + 25e \rightarrow 3CuInSe_2 + 12H_2O \tag{15}$$

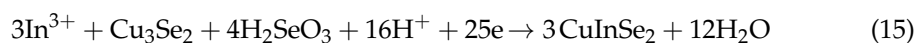$$3In^{3+} + Cu_3Se_2 + 4H_2Se + e \rightarrow 3CuInSe_2 + 8H^+ \tag{16}$$

Figure 4e illustrates the LSV curves of Cu-Ga-Se ternary solutions at 3 kPa. Peaks C_1, C_2, C_3, and C_4 corresponded to the formation of Cu^+, Se, Cu_3Se_2, and Ga_2Se_3, respectively (Equations (2), (5), (8)–(11) and (14)). Ga^{3+} was induced by $Cu_3Se_2 + H_2SeO_3$

or $Cu_3Se_2 + H_2Se$ to produce $CuGaSe_2$ [31] (Equations (17) and (18)) at peak C_4. As the polarization potential increased, the current density became greater at 3 kPa, indicating that the formation of CGS was promoted in a vacuum environment.
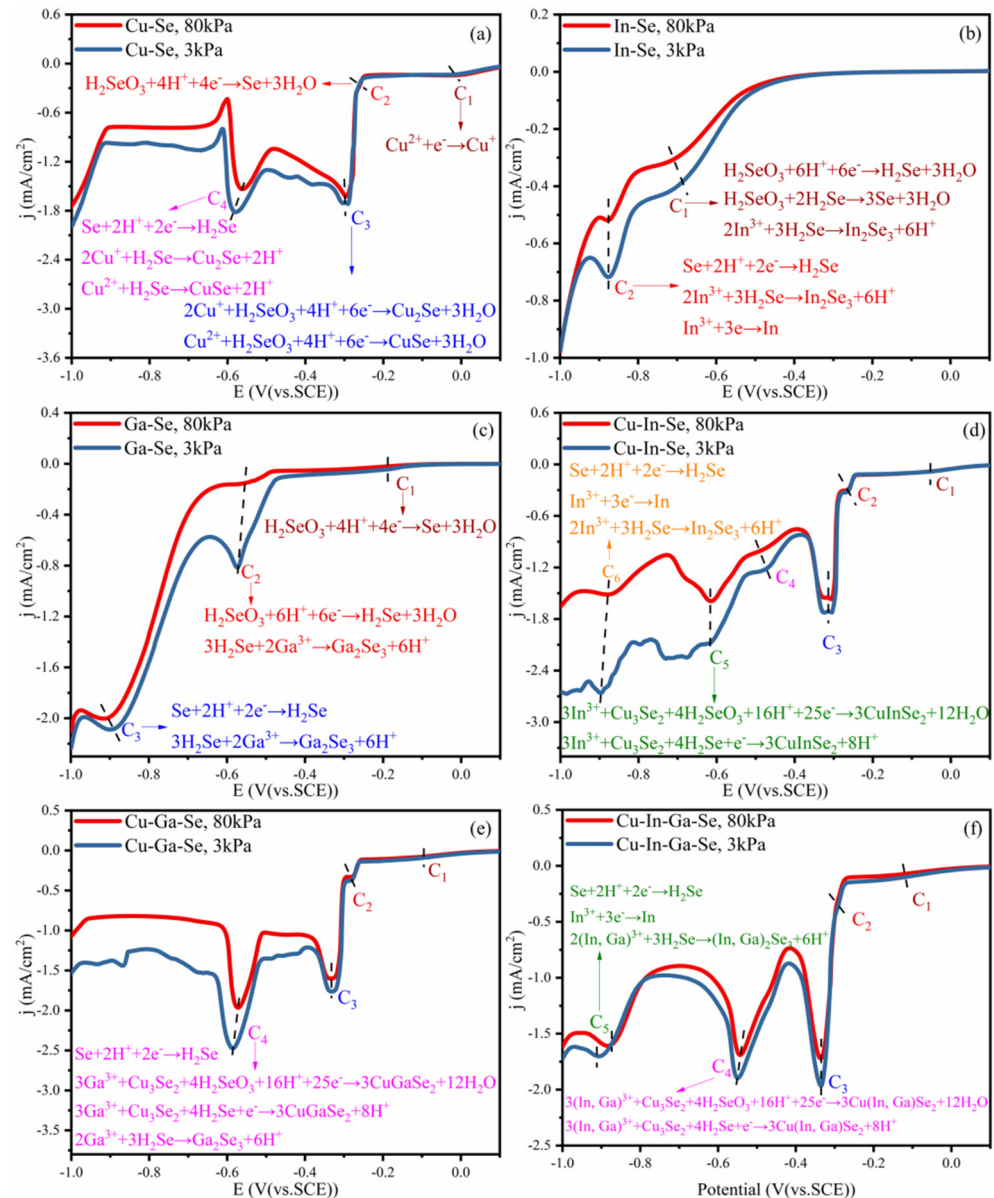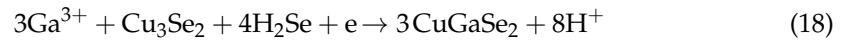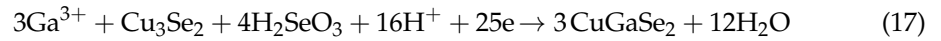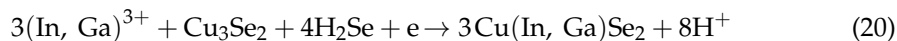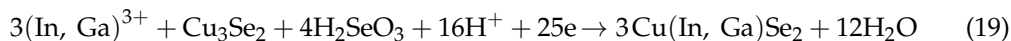
$$3Ga^{3+} + Cu_3Se_2 + 4H_2SeO_3 + 16H^+ + 25e \rightarrow 3\,CuGaSe_2 + 12H_2O \qquad (17)$$

$$3Ga^{3+} + Cu_3Se_2 + 4H_2Se + e \rightarrow 3\,CuGaSe_2 + 8H^+ \qquad (18)$$

Figure 4. The LSV curves in the (**a**) Cu−Se, (**b**) In−Se (**c**) Ga−Se binary, (**d**) Cu−In−Se, (**e**) Cu−Ga−Se ternary, and (**f**) Cu−In−Ga−Se quaternary solutions at 3 kPa.

Figure 4f illustrates the LSV curves of Cu-In-Ga-Se ternary solutions at 3 kPa. Peaks C_1, C_2, and C_3 corresponded to the formation of Cu^+, Se, and Cu_3Se_2, respectively (Equations (2), (5), (8)–(11)). Ga and In are homotopic elements, and their reduction processes at the cathode are similar (noted as $(In, Ga)^{3+}$ phase). Meanwhile, both In^{3+} and Ga^{3+} were induced by $Cu_3Se_2 + H_2SeO_3$ or $Cu_3Se_2 + H_2Se$ into the films (Equations (15)–(18)). Therefore, In^{3+} and Ga^{3+} competed for reduction at the cathode. According to previous conclusions, the reduction potential of In and Ga in the CIGS thin films was −0.6 V. Therefore, peak C_4 corresponded to the formation of $CuInSe_2$, $CuGaSe_2$, or $Cu(In, Ga)Se_2$

(Equations (19) and (20)). Peak C_5 corresponded to the formation of In_2Se_3, Ga_2Se_3, or In (Equations (13), (14), or (4)). The current density of peak C_4 was greater at 3 kPa, indicating that the formation of CIGS was promoted in a vacuum environment.

$$3(In, Ga)^{3+} + Cu_3Se_2 + 4H_2SeO_3 + 16H^+ + 25e \rightarrow 3Cu(In, Ga)Se_2 + 12H_2O \quad (19)$$

$$3(In, Ga)^{3+} + Cu_3Se_2 + 4H_2Se + e \rightarrow 3Cu(In, Ga)Se_2 + 8H^+ \quad (20)$$

3.2. Potentiostatic Polarization and EIS Analyses

According to the previous conclusion, the main reduction potential of In^{3+} and Ga^{3+} in the CIGS thin films was -0.6 V. Therefore, the potentiostatic polarization potential was set to -0.6 V. Figure 5a illustrates the potentiostatic polarization curve of the CIGS thin films at 3 kPa. The current density was always greater at 3 kPa, indicating that the resistance during the preparation of CIGS thin films was lower in a vacuum environment.
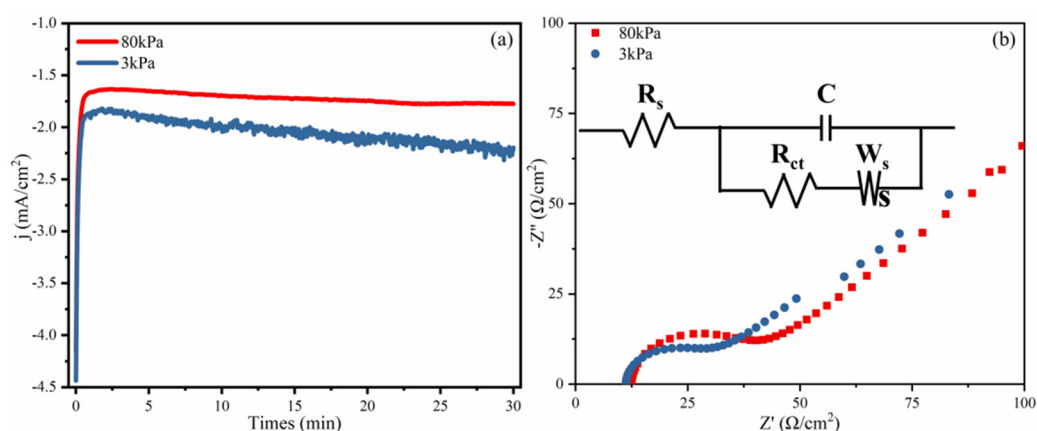
Figure 5. The (**a**) current density−time curve and (**b**) impedance Nyquist plot of electrodeposition CIGS thin films at 3 kPa.

Changes in the diffusion impedance and charge-transfer impedance during the preparation of CIGS thin films were investigated by EIS at a low pressure. Figure 5b illustrates the impedance Nyquist plot of the CIGS thin films deposition process at 3 kPa. The semicircle diameter of the curve was smaller, and the slope of the straight line was larger at 3 kPa, indicating that the electroreduction and diffusion impedances were lower, respectively. In addition, the ohmic impedance was smaller. Thus, the resistance was lower when applying vacuum electrodeposition. This corresponds to the conclusion of the current density-time curves. Both curves in Figure 5b were semicircular with straight lines, indicating that electroreduction and diffusion controlled the CIGS thin films deposition [33].

In this study, the impedance test data were combined in order to fit the equivalent circuit of the CIGS thin films deposition process. The fitted EIS data of the CIGS thin films deposition process at different pressures are shown in Table 1. W_s is the Warburg diffusion impedance, R_{ct} is the charge-transfer impedance between the interface of cathode and electrolyte solutions, C is the electrical double-layer capacitance on the electrode surface, and R_s is the electrolyte solution impedance.

Table 1. Fitting data of CIGS thin films deposition impedance at 3 kPa (Ω).

Pressure	W_s	R_{ct}	C	R_s
80 kPa	417.6	42.39	2.292×10^{-4}	18.77
3 kPa	129.1	29.83	3.546×10^{-4}	19.23

When the system pressure was reduced from 80 kPa to 3 kPa, W_s fell by 69.1%, R_{ct} fell by 29.6%, C rose by 35.4%, and R_s remained constant. Figure 6 illustrates the OER on

the anode surface during the preparation of the CIGS thin films. At 3 kPa, the number of bubbles at the Pt electrode was higher, and the volume was larger. Therefore, the formation of O_2 was promoted under a vacuum. The promoted formation of O_2 indicates that the electrode reaction proceeded more smoothly. The smooth occurrence of the electrode reaction was also one of the reasons for the higher current density at 3 kPa. In addition, according to Boyle's law, the bubble volume should be larger in a vacuum environment. This is consistent with the phenomenon in Figure 6. The rapid release of O_2 bubbles enhanced the diffusion of the electrolyte solution. Therefore, the W_s value fell. Since the reaction of H^+ to H_{ads} was inhibited, and the rapid dehydrogenation occurred in the electrolyte at 3 kPa, the contact area increased between the interface of the cathode and electrolyte solution, which decreased the R_{ct} value. Because the reaction of H^+ to H_{ads} was inhibited, the deposition of major elements increased. Thus, the thickness of the CIGS thin films increased, which increased the C value at 3 kPa. Because it was determined by the electrolyte solution, the R_s value remained constant.
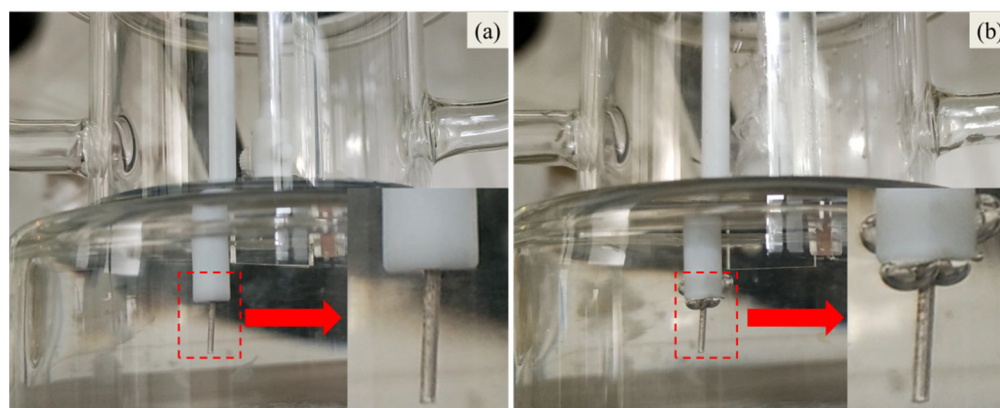
Figure 6. The picture of the OER on the anode surface at pressures of (**a**) 80 kPa and (**b**) 3 kPa.

3.3. EDS Analysis

Figure 7 illustrates the EDS composition curves of Cu, In, Ga, and Se in CIGS thin films at polarization potentials from -0.1 V to -0.9 V. Overall, changing the pressure had little effect on the element deposition pattern but had a significant impact on the elemental content. Combined with Figure 3, the first reduction potentials of Cu and Se were 0 V and -0.2 V, respectively. Therefore, Cu ions were more easily reduced when the reduction potential was -0.1 V. As shown in Figure 7a, the content of Cu in the films was highest at this time. The formation of Cu and Cu_3Se_2 was promoted in a vacuum environment, which in turn led to a high content of Cu in the films at 3 kPa. When the reduction potential was -0.2 V, the reduction of Se became easier. As shown in Figure 7d, the content of Se in the films increased. As the potential increases, the Cu and Se content tended to be relatively stable. As a whole, the content of Cu and Se in the CIGS thin films was slightly higher at 3 kPa, indicating that the vacuum environment was beneficial for the formation of Cu and Se.

As shown in Figure 7b, the potential of In in the CIGS thin films was -0.2 V at 3 kPa. However, this potential was -0.4 V at 80 kPa. The reason may be that the formation of Cu_3Se_2 was promoted in a vacuum environment and In was induced by the excess Cu_3Se_2 to produce a more stable $CuInSe_2$ phase, which in turn could enter the films at a lower potential. Meanwhile, the content of In in the films was higher at 3 kPa. As a result, the formation of In was promoted in a vacuum environment.

As shown in Figure 7c, when the potential was lower, the formation of Ga was largely unaffected due to the lower In content in the films. Because the In content in the films increased as the potential increased, and the formation of In and Ga had a competitive relationship, the formation of Ga was inhibited. This was the first reason for the low concentration of Ga in the CIGS thin films at 3 kPa. Upon increasing the potential, the

production of H_2 at the cathode surface increased at 80 kPa. In turn, the consumption of H^+ in the cathode region increased. Along with the consumption of H^+, the pH at the cathode region increased, which led to the hydrolysis of Ga^{3+} to Ga_2O_3 [24]. Ga^{3+} entered the films in the form of Ga_2O_3 [23]. Because the reaction of H^+ to H_{ads} was inhibited and the OER was promoted at 3 kPa, the pH remained relatively stable at the cathode region, which prevented Ga^{3+} from entering the films in the form of Ga_2O_3. This was the second reason for the low Ga concentration in the CIGS thin films at 3 kPa. In summary, the formation of Ga was inhibited in a vacuum environment.
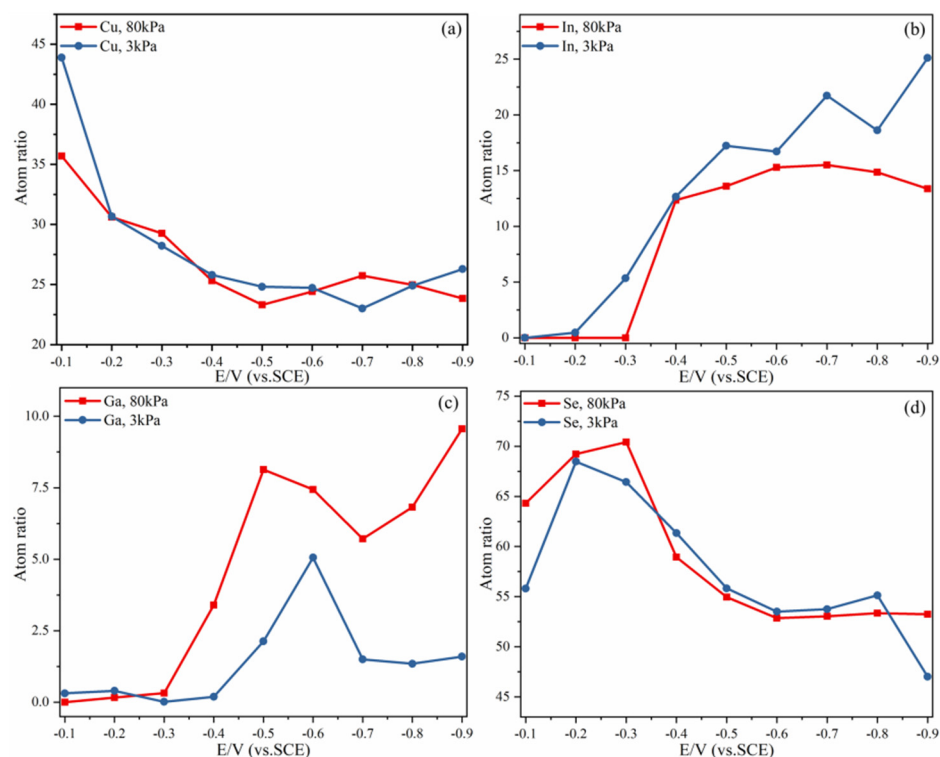

Figure 7. EDS composition curves of (**a**) Cu, (**b**) In, (**c**) Ga, and (**d**) Se in CIGS thin films.

3.4. Morphologic Analyses

SEM images showing the morphologies of the CIGS thin films prepared at various deposition potentials and pressures are displayed in Figure 8. Overall, the particles [29] in the films were larger at 3 kPa. The first reason is that the reaction of H^+ to H_{ads} was inhibited, which in turn inhibited H_2 production. Another reason is that the vacuum environment quickly removed H_2 from the surface of the CIGS thin films. The amount of H_2 adsorbed on the cathode surface decreased, and the space available for the deposition of major elements increased.

3.5. Phase Analyses

As shown in Figure 9, in the CIGS thin films, there are three main diffraction peaks due to (101), (112), and (220) planes corresponding to $CuIn_{0.7}Ga_{0.3}Se_2$. The positions of these diffraction peaks are quite similar. In addition, the difference in pressure changes the preferred crystallographic orientation. When the pressure is 80 kPa, the $CuIn_{0.7}Ga_{0.3}Se_2$ phase possesses a (101) preferred crystallographic orientation at approximately $17.27°$. However, under 3 kPa, the preferred crystallographic orientation is a (112) plane located at approximately $26.90°$. For the $CuIn_{0.7}Ga_{0.3}Se_2$ phase, a preference for the (112) plane is more favorable. Therefore, the main $CuIn_{0.7}Ga_{0.3}Se_2$ phase can be electrochemically deposited at the pressure of 80 kPa and even at 3 kPa, although with different preferred crystallographic orientations.
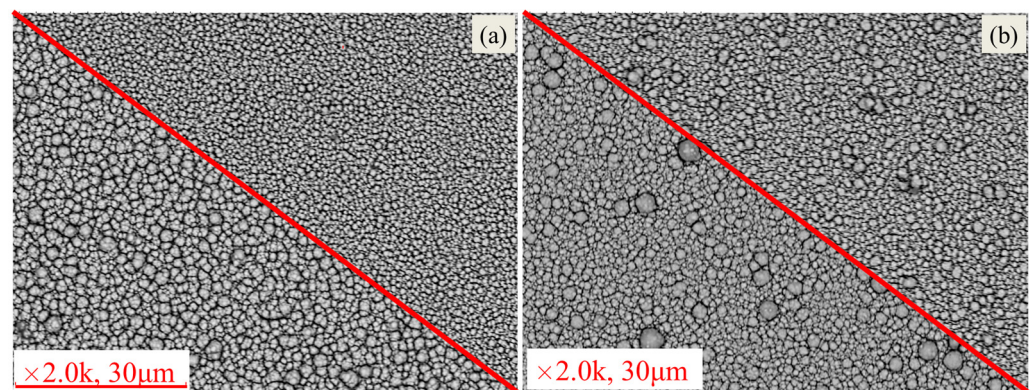
Figure 8. SEM images of the morphology of CIGS thin films prepared at the pressures of 80 kPa (above the red diagonal line) and 3 kPa (below the red diagonal line) and at the potentials of (**a**) −0.5 V and (**b**) −0.6 V.
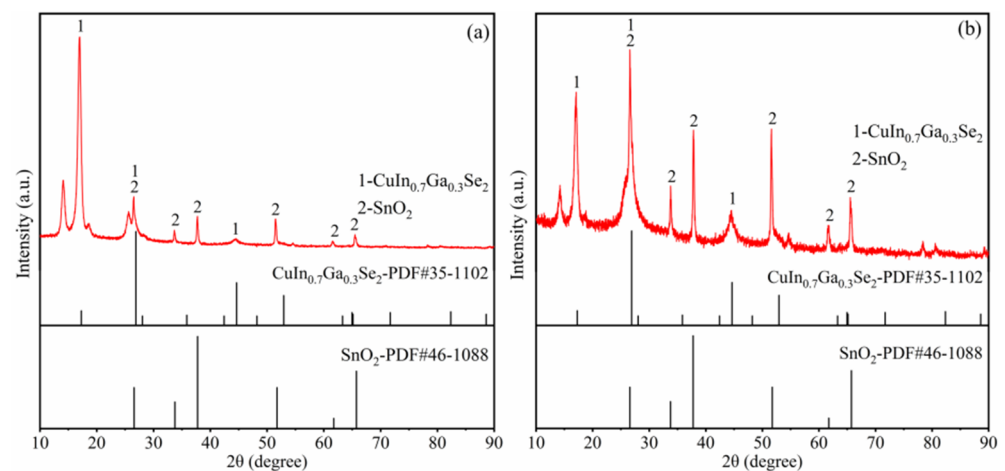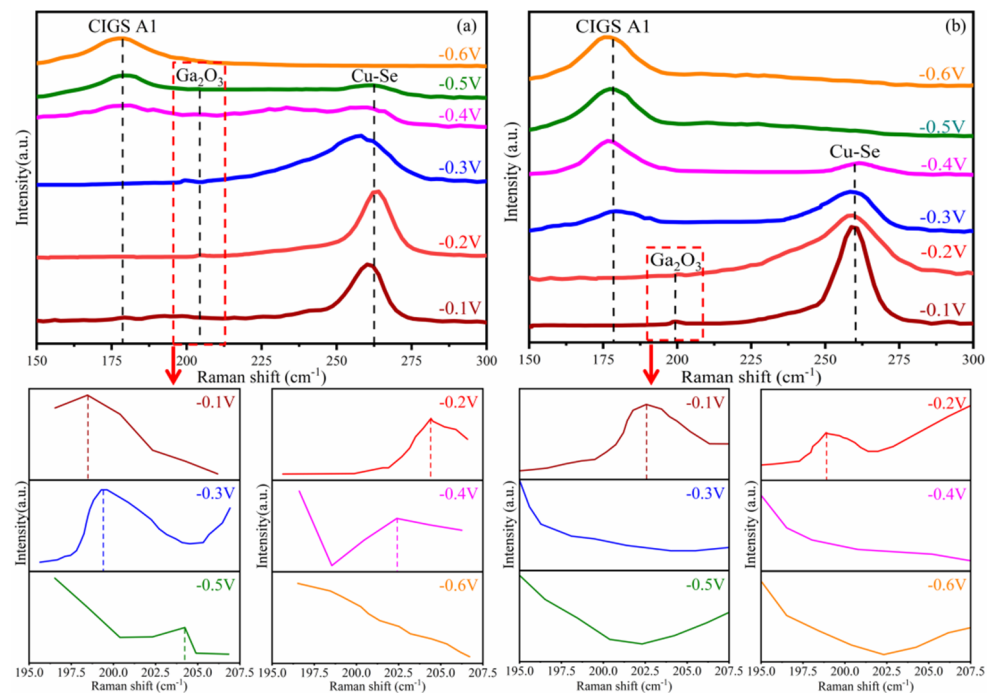

Figure 9. XRD spectra of CIGS thin film prepared at the potential of −0.6 V and pressures of: (**a**) 80 kPa and (**b**) 3 kPa.

The surface phases were characterized by Raman spectroscopy, as shown in Figures 10 and 11. According to Figure 10a, the vibrational peaks of the Ga_2O_3 phase (200 cm^{-1} [34]) appeared in the potential range from −0.1 V to −0.2 V at both 80 kPa and 3 kPa. This was because the reaction of H_2SeO_3 to Se consumed H$^+$ in the cathode region, which in turn hydrolyzed Ga to Ga_2O_3 in the films [35]. Meanwhile, little O_2 formed on the anode surface due to the low potential and could not increase the mass transfer rate of the solution at 3 kPa. This was why the Ga_2O_3 phase appeared at a low potential at 3 kPa.

When the potential was −0.3 V, the main phase of the films changed from the Cu-Se phase (260 cm^{-1} [36]) to the CIGS A1 phase (175 cm^{-1} [37]) at 3 kPa. The formation of the CIGS A1 phase led to a decrease in the consumption of H$^+$. Increasing the potential led to a gradual increase in the O_2 production, which in turn led to a gradual increase in the mass transfer rate, resulting in a stable pH in the cathode region. Ga^{3+} hydrolysis was inhibited, and the Ga_2O_3 phase disappeared. However, at 80 kPa, when the potential was −0.4 V, only the main phase of the films began to transform. In correspondence with the higher potential, the hydrogen evolution reaction began to occur. Therefore, the vibrational peak of the Ga_2O_3 phase was always present when the potential was in the range of −0.3 V to −0.5 V.

As shown in Figure 11, Ga entered the films as Ga-Se phase (214 cm^{-1} [38]) at 3 kPa. Combined with the above conclusions, the formation of Ga_2O_3 was inhibited at 3 kPa.

Figure 10. Raman spectra of CIGS thin film prepared at potentials of −0.1 V to −0.6 V and pressures of: (**a**) 80 kPa and (**b**) 3 kPa.
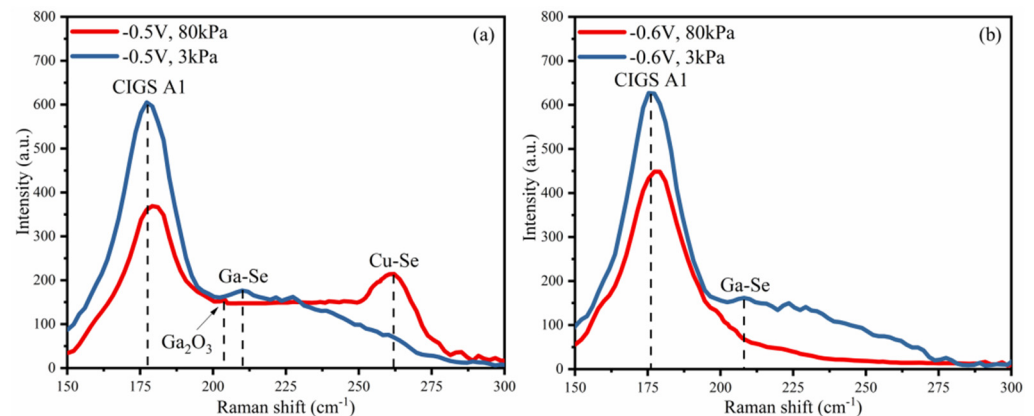
Figure 11. Raman spectra of CIGS thin films prepared at pressures of 80 kPa and 3 kPa and at potentials of (**a**) −0.5 V and (**b**) −0.6 V.

Since poorly-crystallized Ga_2O_3 did not produce a Raman response, this article determined the phase of Ga from the Ga 3d binding energy. The XPS spectra of the CIGS thin films are presented in Figure 12. According to Figure 11, at 80 kPa, the binding energy of 19.73 eV and 20.51 eV are related to Ga of CIGS thin films, and at 3 kPa, 19.07 eV and 19.87 eV are related to Ga of CIGS thin films. According to the literature, 19.07 eV corresponds to GaSe (19.00 eV, Ga 3d) [39], and 19.73 eV and 19.87 eV correspond to Ga_2Se_3 (19.70 eV or 19.90 eV, Ga 3d5/2) [40]. In addition, 20.51 eV is close to Ga_2O_3 (20.50 eV, Ga 3d5/2) [41]. In summary, the phases of the films were Ga_2Se_3 and Ga_2O_3 at 80 kPa, while GaSe and Ga_2Se_3 were the phases at 3 kPa. That is to say, the formation of Ga_2O_3 must be inhibited in a vacuum environment.
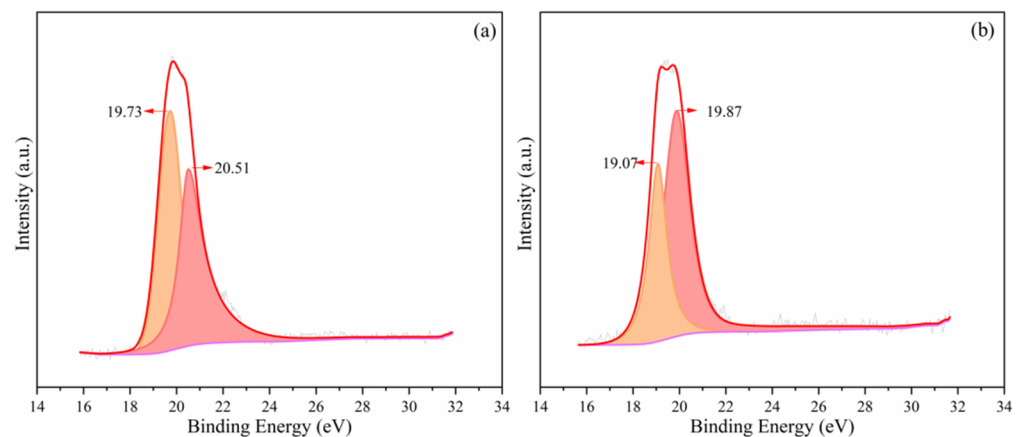
Figure 12. Binding energy of Ga 3d in CIGS thin films prepared at the potential of −0.6 V and pressures of (**a**) 80 kPa and (**b**) 3 kPa.

4. Conclusions

In this article, CIGS films without a low-conductivity Ga_2O_3 phase were prepared using vacuum electrodeposition, as supported by the conclusions of Raman and XPS. There were two main reasons for the inhibited Ga_2O_3 formation. The first reason is the inhibition of the H^+ to H_{ads} reaction, which decreased the consumption of H^+ on the cathode surface, as confirmed by the disappearance of the H_{ads} generation peak in the LSV curve. The second reason is that the OER reaction was promoted by a smoother electrode reaction and a decrease in the electrochemical impedance during deposition. The larger current density in the current density-time curves and the smaller semicircle diameter in the impedance Nyquist plots confirmed this. The inhibition of the H^+ to H_{ads} reaction and the promotion of the OER together stabilized the pH in the cathode region, which in turn inhibited Ga^{3+} hydrolysis. The path of Ga^{3+} into the films in the form of Ga_2O_3 was blocked.

In a vacuum environment, the content of Cu, In, and Se in the films increased, the current density of the preparation process increased, and the resistance decreased. The increase in the deposition space of the main elements produced larger particles in the films.

Data Availability Statement: The data presented in this study are available on request from the corresponding author. The data are not publicly available due to unfinished related ongoing further studies.

References

1. Kang, C.; Lee, G.; Lee, W.; Cho, D.H.; Maeng, I.; Chung, Y.D.; Kee, C.S. Terahertz Emission and Ultrafast Carrier Dynamics of Ar-Ion Implanted Cu(In, Ga)Se$_2$ Thin Films. *Crystals* **2021**, *11*, 411. [CrossRef]
2. Jiang, J.; Giridharagopal, R.; Jedlicka, E.; Sun, K.; Yu, S.; Wu, S.; Gong, Y.; Yan, W.; Ginger, D.S.; Green, M.A.; et al. Highly efficient copper-rich chalcopyrite solar cells from DMF molecular solution. *Nano Energy* **2020**, *69*, 104438. [CrossRef]

3. Hedayati, M.; Olyaee, S. High-Efficiency p-n Homojunction Perovskite and CIGS Tandem Solar Cell. *Crystals* **2022**, *12*, 703. [CrossRef]

4. Huang, C.H.; Chuang, W.J.; Lin, C.P.; Jan, Y.L.; Shih, Y.C. Deposition Technologies of High-Efficiency CIGS Solar Cells: Development of Two-Step and Co-Evaporation Processes. *Crystals* **2018**, *8*, 296. [CrossRef]

5. Ma, Q.; Zhang, W.; Jiang, Z.; Ma, D.; Zhang, Y.; Lu, C.; Fan, Z. The Formation Mechanism of $Cu(In_{0.7}Ga_{0.3})Se_2$ Nanoparticles and the Densification Trajectory of the Se-Rich Quaternary Target by Hot Pressing. *Crystals* **2018**, *8*, 135. [CrossRef]

6. Altaf, C.T.; Sahsuvar, N.S.; Abdullayeva, N.; Coskun, O.; Kumtepe, A.; Karagoz, E.; Sankir, M.; Sankir, N.D. Inverted Configuration of $Cu(In, Ga)S_2/In_2S_3$ on 3D-ZnO/$ZnSnO_3$ Bilayer System for Highly Efficient Photoelectrochemical Water Splitting. *ACS. Sustain. Chem. Eng.* **2020**, *8*, 15209–15222. [CrossRef]

7. Matur, U.C.; Baydogan, N. Changes in gamma attenuation behaviour of sol-gel derived CIGS thin film irradiated using Co-60 radioisotope. *J. Alloys Compd.* **2017**, *695*, 1405–1413. [CrossRef]

8. Ao, J.; Fu, R.; Jeng, M.J.; Bi, J.; Yao, L.; Gao, S.; Sun, G.; He, Q.; Zhou, Z.; Sun, Y.; et al. Formation of Cl-Doped ZnO Thin Films by a Cathodic Electrodeposition for Use as a Window Layer in CIGS Solar Cells. *Materials* **2018**, *11*, 953. [CrossRef]

9. Oliveri, R.L.; Patella, B.; Pisa, F.D.; Mangione, A.; Aiello, G.; Inguanta, R. Fabrication of CZTSe/CIGS Nanowire Arrays by One-Step Electrodeposition for Solar-Cell Application. *Materials* **2021**, *14*, 2778. [CrossRef]

10. Péter, L.; Fekete, É.; Kapoor, G.; Gubicza, J. Influence of the preparation conditions on the microstructure of electrodeposited nanocrystalline Ni–Mo alloys. *Electrochim. Acta* **2021**, *382*, 138352. [CrossRef]

11. Beltowska-Lehman, E.; Bigos, A.; Indyka, P.; Kot, M. Electrodeposition and characterisation of nanocrystalline Ni–Mo coatings. *Surf. Coat. Technol.* **2012**, *211*, 67–71. [CrossRef]

12. Ren, Y.; Ma, W.; Wei, K.; Yu, W.; Dai, Y.; Morita, K. Degassing of aluminum alloys via the electromagnetic directional solidification. *Vacuum* **2014**, *109*, 82–85. [CrossRef]

13. Fromm, E. Maximum rate of sorption and degassing processes in vacuum metallurgical treatments. *Vacuum* **1971**, *21*, 585–586. [CrossRef]

14. Pessel, L. Apparatus for electroplating metal. U.S. Patent 2465747, 30 April 1945.

15. Muttilainen, E.; Tunturi, P.J. Hard chromium plating under reduced pressure improves corrosion resistance. *Anti-Corros. Method. M.* **1984**, *31*, 13–15. [CrossRef]

16. Nam, S.E.; Lee, S.H.; Lee, K.H. Preparation of a palladium alloy composite membrane supported in a porous stainless steel by vacuum electrodeposition. *J. Membrane. Sci.* **1999**, *153*, 163–173. [CrossRef]

17. Nam, S.E.; Seong, Y.K.; Lee, J.W.; Lee, K.H. Preparation of highly stable palladium alloy composite membranes for hydrogen separation. *Desalination* **2007**, *236*, 51–55. [CrossRef]

18. Su, R.; Lü, Z.; Chen, K.; Ai, N.; Li, S.; Wei, B.; Su, W. Novel in situ method (vacuum assisted electroless plating) modified porous cathode for solid oxide fuel cells. *Electrochem. Commun.* **2008**, *10*, 844–847. [CrossRef]

19. Ming, P.; Zhu, D.; Hu, Y.; Zeng, Y. Micro-electroforming under periodic vacuum-degassing and temperature-gradient conditions. *Vacuum* **2009**, *83*, 1191–1199. [CrossRef]

20. Ming, P.; Li, Y.; Wang, S.; Li, S.; Li, X. Microstructure and properties of nickel prepared by electrolyte vacuum boiling electrodeposition. *Surf. Coat. Technol.* **2012**, *213*, 299–306. [CrossRef]

21. Hibberd, C.J.; Chassaing, E.; Liu, W.; Mitzi, D.B.; Lincot, D.; Tiwari, A.N. Non-vacuum methods for formation of Cu(In, Ga)(Se, S)$_2$ thin film photovoltaic absorbers. *Prog. Photovoltaics.* **2010**, *18*, 434–452. [CrossRef]

22. Estela Calixto, M.; Dobson, K.D.; McCandless, B.E.; Birkmire, R.W. Controlling Growth Chemistry and Morphology of Single-Bath Electrodeposited $Cu(In, Ga)Se_2$ Thin Films for Photovoltaic Application. *J. Electrochem. Soc.* **2006**, *153*, G521–G528. [CrossRef]

23. Yang, J.; Huang, C.; Jiang, L.; Liu, F.; Lai, Y.; Li, J.; Liu, Y. Effects of hydrogen peroxide on electrodeposition of $Cu(In, Ga)Se_2$ Thin films and band gap controlling. *Electrochim. Acta* **2014**, *142*, 208–214. [CrossRef]

24. Flamini, D.O.; Saidman, S.B.; Bessone, J.B. Electrodeposition of gallium onto vitreous carbon. *J. Appl. Electrochem.* **2007**, *37*, 467–471. [CrossRef]

25. Murray, R.; Sigmund, S. The H^+/H_2 equilibrium potential dependence on H_2 partial pressure on gold electrodes. *Electrochim. Acta* **1973**, *18*, 687–690.

26. Warner, T.B.; Schuldiner, S. Potential of a Platinum Electrode at Low Partial Pressures of Hydrogen or Oxygen. *J. Electrochem. Soc.* **1965**, *112*, 853–856. [CrossRef]

27. Liu, J.; Liu, F.; Lai, Y.; Zhang, Z.; Li, J.; Liu, Y. Effects of sodium sulfamate on electrodeposition of Cu(In, Ga)Se$_2$ thin film. *Electroanal. Chem.* **2011**, *651*, 191–196. [CrossRef]

28. Lai, Y.; Liu, F.; Zhang, Z.; Liu, J.; Li, Y.; Kuang, S.; Li, J.; Liu, Y. Cyclic voltammetry study of electrodeposition of $Cu(In, Ga)Se_2$ thin films. *Electrochim. Acta* **2008**, *54*, 3004–3010. [CrossRef]

29. Lincot, D.; Guillemoles, J.F.; Taunier, S.; Guimard, D.; Sicx-Kurdi, J.; Chaumont, A.; Roussel, O.; Ramdani, O.; Hubert, C.; Fauvarque, J.P.; et al. Chalcopyrite thin film solar cells by electrodeposition. *Sol. Energy.* **2004**, *77*, 725–737. [CrossRef]

30. Lai, Y.; Liu, J.; Yang, J.; Wang, B.; Liu, F.; Zhang, Z.; Li, J.; Liu, Y. Incorporation Mechanism of Indium and Gallium during Electrodeposition of $Cu(In, Ga)Se_2$ Thin Film. *J. Electrochem. Soc.* **2011**, *158*, D704–D709. [CrossRef]

31. Lai, Y.; Liu, F.; Li, J.; Zhang, Z.; Liu, Y. Nucleation and growth of selenium electrodeposition onto tin oxide electrode. *Electroanal. Chem.* **2010**, *639*, 187–192. [CrossRef]

32. Kemell, M.; Ritala, M.; Saloniemi, H.; Leskelä, M.; Sajavaara, T.; Rauhala, E. One-Step Electrodeposition of $Cu_{2-x}Se$ and $CuInSe_2$ Thin Films by the Induced Co-deposition Mechanism. *J. Electrochem. Soc.* **2000**, *147*, 1080–1087. [CrossRef]

33. You, R.; Lew, K.K.; Fu, Y.P. Effect of indium concentration on electrochemical properties of electrode-electrolyte interface of $CuIn_{1-x}Ga_xSe_2$ prepared by electrodeposition. *Mater. Res. Bull.* **2017**, *96*, 183–187. [CrossRef]

34. Gonzalo, A.; Nogales, E.; Lorenz, K.; Víllora, E.G.; Shimamura, K.; Piqueras, J.; Méndez, B. Raman and cathodoluminescence analysis of transition metal ion implanted Ga_2O_3 nanowires. *J. Lumin.* **2017**, *191*, 56–60. [CrossRef]

35. Liu, F.; Yang, J.; Zhou, J.; Lai, Y.; Jia, M.; Li, J.; Liu, Y. One-step electrodeposition of $CuGaSe_2$ thin films. *Thin Solid Films* **2012**, *520*, 2781–2784. [CrossRef]

36. Ren, T.; Yu, R.; Zhong, M.; Shi, J.; Li, C. Microstructure evolution of $CuInSe_2$ thin films prepared by single-bath electrodeposition. *Sol. Energ. Mat. Sol. C* **2010**, *95*, 510–520. [CrossRef]

37. Insignares-Cuello, C.; Izquierdo-Roca, V.; López-García, J.; Calvo-Barrio, L.; Saucedo, E.; Kretzschmar, S.; Unold, T.; Broussillou, C.; Goislard de Monsabert, T.; Bermudez, V.; et al. Combined Raman scattering/photoluminescence analysis of Cu(In, Ga)Se_2 electrodeposited layers. *Solar Energy* **2014**, *103*, 89–95. [CrossRef]

38. Bergeron, A.; Ibrahim, J.; Leonelli, R.; Francoeur, S. Oxidation dynamics of ultrathin GaSe probed through Raman spectroscopy. *Appl. Phys. Lett.* **2017**, *110*, 241901. [CrossRef]

39. Lang, O.; Tomm, Y.; Schlaf, R.; Pettenkofer, C.; Jaegermann, W. Single crystalline GaSe/WSe_2 heterointerfaces grown by van der Waals epitaxy. II. Junction characterization. *J. Appl. Phys.* **1994**, *75*, 7814–7820. [CrossRef]

40. Iwakuro, H.; Tatsuyama, C.; Ichimura, S. XPS and AES Studies on the Oxidation of Layered Semiconductor GaSe. *Jpn. J. Appl. Phys.* **1982**, *21*, 94–99. [CrossRef]

41. Carli, R.; Bianchi, C.L. XPS analysis of gallium oxides. *Appl. Surf. Sci.* **1994**, *74*, 99–102. [CrossRef]